Intense monochromatic photons above 100 keV from an inverse Compton source

Kirsten Deitrick[®] and Georg H. Hoffstaetter[®]

Cornell Laboratory for Accelerator Based Sciences and Education, Cornell University, Ithaca, New York 14850, USA

Carl Franck

Laboratory of Atomic and Solid State Physics, Cornell University, Ithaca, New York 14850, USA

Bruno D. Muratori and Peter H. Williams

STFC Daresbury Laboratory & Cockcroft Institute, Warrington WA4 4AD, United Kingdom

Geoffrey A. Krafft®

Department of Physics, Center for Accelerator Science, Old Dominion University, Norfolk, Virginia 23529, USA

Thomas Jefferson National Accelerator Facility, Newport News, Virginia 23606, USA

Balša Terzić

Department of Physics, Center for Accelerator Science, Old Dominion University, Norfolk, Virginia 23529, USA

Joe Crone and Hywel Owen

Department of Physics, University of Manchester & Cockcroft Institute, Manchester M13 9PL, United Kingdom

(Received 8 September 2020; accepted 27 April 2021; published 27 May 2021)

Quasimonochromatic x rays are difficult to produce above 100 keV, but have a number of uses in x-ray and nuclear science, particularly in the analysis of transuranic species. Inverse Compton scattering (ICS) is capable of fulfilling this need, producing photon beams with properties and energies well beyond the limits of typical synchrotron radiation facilities. We present the design and predicted output of such an ICS source at CBETA, a multiturn energy-recovery linac with a top energy of 150 MeV, which we anticipate producing x rays with energies above 400 keV and a collimated flux greater than 108 photons per second within a 0.5% bandwidth. At this energy, the anticipated flux exceeds that attainable from storage ring sources of synchrotron radiation, even though CBETA is a significantly smaller accelerator system. We also consider the consequences of extending the CBETA ICS source performance to higher electron energies, exploring achievable parameters and applications for MeV-scale photons. We foresee that future energy-recovery linacs may serve as ICS sources, capable of providing high energy photons unavailable at synchrotron radiation facilities or photon beams above approximately 300 keV which outperform sources at synchrotron radiation facilities in both flux and average brilliance.

DOI: 10.1103/PhysRevAccelBeams.24.050701

Published by the American Physical Society under the terms of the Creative Commons Attribution 4.0 International license. Further distribution of this work must maintain attribution to the author(s) and the published article's title, journal citation, and DOI.

I. INTRODUCTION

Intense sources of high-energy photons above 1 keV can be obtained in the laboratory in one of four practical ways: discrete line gamma sources from radioactive decay, bremsstrahlung of electrons within a solid target, synchrotron radiation (SR), and inverse Compton scattering (ICS). Such sources are today the mainstay of many areas of

kd324@cornell.edu

scientific study. Storage ring production of narrow-band undulator x rays from 1 to 100 keV (which requires GeV-scale electrons) has very broad use across many topics including diffraction and spectroscopy; broadband brems-strahlung from lower-energy electrons (typically tens of MeV) finds application in imaging and nuclear physics, particularly when applied to the identification and quantification of nuclear materials using MeV-scale photons. Bremmsstrahlung sources are technically convenient but not ideal due to their inherent large photon energy spread.

Important techniques using high-energy photons are x-ray absorption spectroscopy [1], x-ray fluorescence (XRF) [1], and nuclear resonance fluorescence (NRF) [2]; for samples with high atomic number Z these have numerous applications in nuclear physics, industry, and nuclear security. For example, a high-Z nucleus such as uranium (Z = 92) has $K\alpha_2$ and $K\alpha_1$ energies of 94.7 and 98.4 keV respectively (K edge energy 115.6 keV)—photons of higher energies are needed to probe transuranic species. Similarly, NRF can be used to discriminate with precision the quantities of transuranic isotopes in large samples (such as spent nuclear fuel canisters) using photons in the 1 to 3 MeV range (for example, 235 U detection needs 1.733 MeV photons) [3].

Bremsstrahlung sources generate a large quantity of unused photons at lower energies that may cause a number of instrumental issues; ideally, a monochromatic (or quasimonochromatic) source is desired. Electron storage rings at the higher practicable stored bunch energies around 6–8 GeV (such as the national facilities ESRF [4], APS [5], and SPRING-8 [6]) can generate intense, monochromatic photons up to approximately 200 keV; while higher energies are possible, they are not typical. However, these sources are hardly compact (the storage rings are around 1 km in circumference), and their output does not readily extend to the MeV scale.

ICS in the head-on geometry using the common 1064 nm incident wavelength (photon energy $E_{\rm laser}=1.17~{\rm eV})$ gives backscattered photons of energy

$$E_{\gamma} = 4\gamma^2 E_{\text{laser}} \tag{1}$$

for electrons with Lorentz factor $\gamma = E_e/m_ec^2$, where m_e is the rest mass of the electron and c is the speed of light. Hence, electrons with energy $E_e \simeq 75$ MeV are needed to produce 100 keV photons, and $E_e \simeq 240$ MeV is needed for 1 MeV photons. With sufficient scattering rate and suitable collimation, ICS sources using moderate electron energy may generate intense MeV-scale photons.

The focus of this paper is to examine the feasibility and benefits of using an energy recovery linac (ERL) driven ICS light source as an intense source of photons unavailable at synchrotron radiation facilities, and provide an example of such a source based on the recently commissioned multiturn ERL utilizing superconducting radio-

frequency (SRF) cavities: CBETA—the Cornell-BNL ERL Test Accelerator [7]. The paper layout is as follows: Sec. II serves as an introduction to the underlying physics and formula of ICS light sources; Sec. III provides an overview of CBETA; Sec. IV describes the design of a bypass line for ICS x-ray production and characterization of the expected photon spectrum; Sec. V compares the anticipated performance of the CBETA ICS to existing radiation sources, including ICS and storage ring sources, demonstrates how modestly extending the CBETA parameters provides a realistic design for MeV-scale photons through ICS, and explores potential applications.

II. INVERSE COMPTON SCATTERING SOURCES

A. Theory of inverse Compton scattering

Following their original description by Feenberg and Primakoff [8], sources based on inverse Compton scattering (ICS)—the process of scattering a photon from a relativistic-moving electron—have emerged as a promising way to generate tunable, monochromatic photons across output energies from tens of keV as far as the GeV scale [9–11]. The energy of the scattered photons—taking into account electron recoil—is given by

$$E_{\gamma} = \frac{E_{\text{laser}}(1 - \beta \cos \phi')}{1 - \beta \cos \theta + (1 - \cos \theta')E_{\text{laser}}/E_e},$$
 (2)

where $E_e = \gamma m_e c^2$ is the incident (total) electron energy, E_{laser} is the incident (laser) photon energy, $\beta = v/c$, v the average speed of the electrons, c the speed of light, θ the angle between the incident electrons and the outgoing scattered photons, and ϕ' the angle between the incident electrons and incident photons. $\theta' = \phi' - \theta$ is the angle between the incident and scattered photons and $\phi = \pi - \phi'$ is the crossing angle. The geometry of the interaction point (IP) and these angles is shown in Fig. 1 [12,13].

The highest-energy photons are produced in a head-on collision between an electron and photon ($\phi' = \pi$), when photons are backscattered into the same direction as the incident electron ($\theta = 0$); this highest photon energy is referred to as the Compton edge. Taking the electron recoil into account, the maximum energy of the scattered photons is given by

$$E_{\gamma}^{\text{max}} = \frac{4\gamma^2 E_{\text{laser}}}{1 + X},\tag{3}$$

where $X = 4\gamma E_{\text{laser}}/m_e c^2$ is the electron recoil parameter [14]. The Thomson regime is when electron recoil is negligible ($X \ll 1$), and the Compton edge energy becomes

$$E_{\gamma}^{\text{max}} = 4\gamma^2 E_{\text{laser}}.$$
 (4)

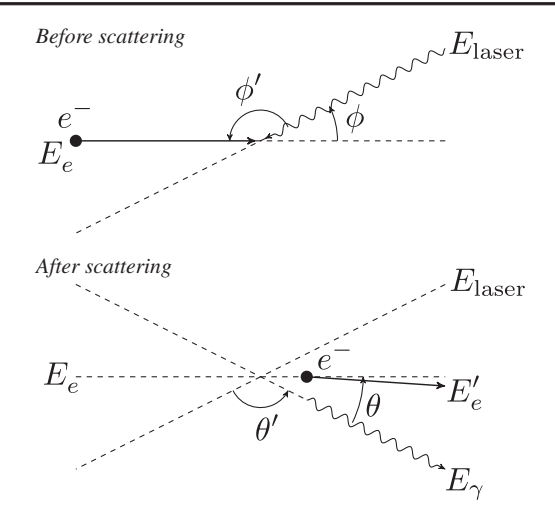


FIG. 1. Geometry of scattering at the inverse Compton scattering interaction point; has the same geometry as Fig. 1 in Sun *et al.* [13].

In this regime, the scattering interaction can be viewed as an elastic collision. Electron recoil becomes significant when both γ and $E_{\rm laser}$ are large, and in this situation

$$E_{\gamma} \to E_e;$$
 (5)

the scattered photon energy cannot have more energy than the incident electron. A practical example of this is the proposed collision of 12 keV FEL photons with 7 GeV electrons within a storage ring ($X \sim 1000$), where the scattered photon energy becomes essentially also 7 GeV [15].

Compton scattering can be treated as analogous to undulator radiation. In that vein, the undulator K-parameter is similar to the laser field strength parameter a_0 for Compton scattering, which is

$$a_0 = \frac{eE\lambda_{\text{laser}}}{2\pi mc^2},\tag{6}$$

where e is the electron charge, E the transverse electric field of the laser, and λ_{laser} is the wavelength of the incident photons. Here we assume the linear regime where $a_0 \ll 1$, and all later formulas continue that assumption [12].

In a collision between an electron bunch (containing N_e electrons) and a laser pulse (containing N_{laser} photons), the total number of scattered photons N_{γ} for a crossing angle ϕ is given by [16]

$$N_{\gamma} = \sigma_c \frac{N_e N_{\text{laser}} \cos(\phi/2)}{2\pi\sigma_v \sqrt{\sigma_x^2 \cos^2(\phi/2) + \sigma_z^2 \sin^2(\phi/2)}}, \quad (7)$$

where σ_c is the Compton scattering cross section and $\sigma_i^2 = \sigma_{\text{electron},i}^2 + \sigma_{\text{laser},i}^2$ is the convoluted spot size of the electron and laser beam in each direction (i = x, y, z) at the interaction point (IP). We note that for the same overlap

of electron and laser spot sizes, the number of Compton-scattered photons is independent of electron energy in the Thomson regime where $\sigma_T \simeq \sigma_c$. The exact Compton cross section from QED [17] is

$$\sigma_c = \sigma_T \frac{3}{4X} \left[\left(1 - \frac{4}{X} - \frac{8}{X^2} \right) \log(1 + X) + \frac{1}{2} + \frac{8}{X} - \frac{1}{2(1 + X)^2} \right], \tag{8}$$

which reduces to

$$\sigma_c \simeq \sigma_T (1 - X),$$
 (9)

for small values of X; $\sigma_T = 6.65 \times 10^{-29} \text{ m}^2 = 8\pi r_e^2/3$ is the Thomson cross section and r_e is the classical electron radius [18]. For $\lambda_{\text{laser}} = 1064$ nm and typical $\gamma \sim 10^3$ we have $X \sim 10^{-2}$, and thus $\sigma_c \simeq \sigma_T$ to the percent level. Assuming the incident laser is approximately a plane wave, the number of scattered photons within a 0.1% bandwidth at the Compton edge is $N_{0.1\%} \simeq 1.5 \times 10^{-3} N_{\gamma}$. Consequently, the rate of photons (flux) into this bandwidth is

$$\mathcal{F}_{0.1\%} \simeq 1.5 \times 10^{-3} \dot{N}_{\gamma},$$
 (10)

where $\dot{N}_{\gamma} = fN_{\gamma} = \mathcal{F}$ is the total uncollimated flux and f is the repetition rate [12]. $N_{0.1\%}$ is independent of electron energy (assuming N_{γ} stays the same) since both $E_{\gamma}^{\rm max}$ and relative bandwidth scale together as γ^2 .

The rms source size [19], $\sigma_{\gamma,j}$, for the scattered photons is given by a convolution of the laser and electron beam spot sizes in the transverse directions (j = x, y)

$$\sigma_{\gamma,j} = \frac{\sigma_{\text{electron},j}\sigma_{\text{laser},j}}{\sqrt{\sigma_{\text{electron},j}^2 + \sigma_{\text{laser},j}^2}}.$$
 (11)

In the nondiffraction-limited case, where the laser spot size at the IP is significantly larger than the electron beam spot size, the average brilliance of the scattered photons (given in conventional units, i.e., mm⁻² mrad⁻² s⁻¹ per 0.1% bandwidth) is

$$\mathcal{B}_{\text{avg}} \approx \frac{\mathcal{F}_{0.1\%}}{4\pi^2 \epsilon^2} = \frac{\gamma^2 \mathcal{F}_{0.1\%}}{4\pi^2 \epsilon_N^2},$$
 (12)

where ϵ is the transverse emittance of the electron beam at the IP and ϵ_N is the normalized transverse emittance, where we assume a round beam. For a more detailed explanation, refer to Deitrick *et al.* [20].

The peak brilliance of the source (for a zero crossing angle) is calculated via an analytical formula of Hartemann *et al.* [21],

$$\begin{split} \mathcal{B}_{\text{peak}} &= 10^{-15} \frac{4\gamma^2}{\pi^2 \epsilon_N^2} \frac{N_e N_L}{\Delta \tau} \frac{r_e^2}{\sigma_{\text{laser}}^2} \\ &\times \exp \left\{ \frac{\chi - 1}{2\chi \Delta u_\perp^2} \left[2 + \frac{\delta \omega^2 + \delta \gamma^2 \chi^2}{2\chi (\chi - 1) \Delta u_\perp^2} \right] \right\} \\ &\times \left\{ 1 - \Phi \left[\frac{\chi - 1}{\sqrt{\delta \omega^2 + \delta \gamma^2 \chi^2}} \left(1 + \frac{\delta \omega^2 + \delta \gamma^2 \chi^2}{2\chi (\chi - 1) \Delta u_\perp^2} \right) \right] \right\} \\ &\times \mathbb{F}(\eta, \mu), \end{split}$$

where $\Delta u_{\perp} = \epsilon_N/\sigma_{\rm electron}$ is the perpendicular velocity spread, $\Delta \tau$ is the electron bunch duration, $\delta \omega$ is the relative frequency spread of the laser, and $\delta \gamma$ is the relative energy spread of the electron beam; the 10^{-15} factor arises as a unit conversion from SI to mm⁻² mrad⁻² s⁻¹ per 0.1% bandwidth. The normalized Doppler up-shifted frequency, χ , is given by

$$\chi = \frac{\omega_x}{4\gamma^2 \omega_0},\tag{14}$$

where ω_x and ω_0 are the angular frequency of the scattered and incident radiation and $\Phi(x)$ is the error function

$$\Phi(x) = \frac{2}{\sqrt{\pi}} \int_0^x e^{-t^2} dt.$$
 (15)

The overlap function $\mathbb{F}(\eta, \mu)$ is given by

$$\mathbb{F}(\eta,\mu) = \frac{\eta e^{1/\eta^2} [1 - \Phi(1/\eta)] - \mu e^{1/\mu^2} [1 - \Phi(1/\mu)]}{\eta^2 - \mu^2}, \quad (16)$$

where $\eta=c\Delta t/2\sqrt{2}\beta^*$ is the normalized inverse β -function, Δt is the laser pulse duration, β^* the (Twiss) β -function at the IP, and $\mu=c\Delta t/2\sqrt{2}z_R$ is the normalized inverse Rayleigh length for a Rayleigh length $z_R=4\pi\sigma_{\rm electron}^2/\lambda$. The spectral density of the scattered photons is given by

$$S = \frac{\mathcal{F}}{E_{\gamma}^{\text{max}}}.$$
 (17)

The combined hourglass and angular crossing $(\phi \neq 0)$ reduction factor R_{ACHG} [22] is given by

$$R_{\text{ACHG}} = \int_{-\infty}^{\infty} \frac{H \exp\left(-hZ_c^2\right)}{\sqrt{\sigma_x^2 + \langle U_x^2 \rangle Z_c^2} \sqrt{\sigma_y^2 + \langle U_y^2 \rangle Z_c^2}} dZ_c, \quad (18)$$

where

$$H = \cos\left(\phi/2\right) \sqrt{\frac{\sigma_x^2 \sigma_y^2}{\pi \sigma_z^2}},\tag{19}$$

$$h = \frac{\sin^2(\phi/2)}{\sigma_x^2 + \langle U_x^2 \rangle Z_c^2} + \frac{\cos^2(\phi/2)}{\sigma_z^2}, \tag{20}$$

and in the case of photon-electron interactions, the divergence term is given by

$$\langle U_j^2 \rangle = \frac{(\sigma_{\text{electron},j}^2 / \beta_j^{*2}) + (\sigma_L^2 / z_R^2)}{2}, \qquad (21)$$

for j = x, y.¹

The angular crossing reduction factor $R_{\rm AC}$ [16,22] is given by

$$R_{\rm AC} = \frac{\sigma_x \cos(\phi/2)}{\sqrt{\sigma_x^2 \cos^2(\phi/2) + \sigma_z^2 \sin^2(\phi/2)}}.$$
 (22)

The primary reduction factor of any ICS interaction—angular crossing or hourglass effect—depends on the specific beam parameters and must be evaluated on a case by case basis.

Using the bandwidth obtained from the scaling laws of N. Ranjan *et al.* [14] and assuming round beams, the bandwidth of the scattered radiation passing through a collimator can be expressed as

(15)
$$\frac{\Delta E_{\gamma}}{E_{\gamma}} = \sqrt{\left(\frac{\sigma_{\theta}}{E_{\theta}}\right)^{2} + \left(\frac{\sigma_{e}}{E_{e}}\right)^{2} + \left(\frac{\sigma_{L}}{E_{L}}\right)^{2} + \left(\frac{\sigma_{\epsilon}}{E_{\epsilon}}\right)^{2}}, \quad (23)$$

where

$$\frac{\sigma_{\theta}}{E_{\theta}} = \frac{1}{\sqrt{12}} \frac{\Psi^2}{1 + X + \Psi^2/2},$$
 (24)

$$\frac{\sigma_e}{E_e} = \frac{2+X}{1+X+\Psi^2} \frac{\Delta E_e}{E_e},\tag{25}$$

$$\frac{\sigma_L}{E_I} = \frac{1 + \Psi^2}{1 + X + \Psi^2} \frac{\Delta E_{\text{laser}}}{E_{\text{laser}}},\tag{26}$$

$$\frac{\sigma_{\epsilon}}{E_{\epsilon}} = \frac{2\gamma\epsilon_N}{(1+X)\beta^*}.$$
 (27)

Here, $\Psi = \gamma \theta_{\rm col}$ is called the acceptance angle, $\theta_{\rm col}$ is the (physical) collimation angle, X is the electron recoil parameter, $\Delta E_e/E_e = \delta \gamma/2$ is the energy spread of the electron beam, $\Delta E_{\rm laser}/E_{\rm laser} = \delta \omega \simeq 6.57 \times 10^{-4}$ is the laser photon energy spread, β^* is the β -function at the IP, and ϵ_N is the normalized emittance of the electron beam at the IP.

This formula allows for the contributions to the bandwidth of the scattered radiation to be separated into individual contributions from collimation Eq. (24), electron

¹Note here that due to a change of crossing angle definition between this work and that of Miyahara [22], Miyahara's ϕ becomes $\phi/2$. Change of notation also means that Miyahara's $\langle \sigma_i^{*2} \rangle$ becomes σ_i^2 for i=x, y, z in our notation.

beam energy spread Eq. (25), laser energy spread Eq. (26), and electron beam emittance Eq. (27). For example, taking a general case of a linac based ICS ($E_e = 100 \text{ MeV}$,

 $\epsilon_N=0.5$ mm mrad, $\Delta E_e/E_e=5\times 10^{-4}$, $\lambda=1064$ nm, $\Delta E_L/E_L=6.57\times 10^{-4}$, $\beta^*=0.1$ m, $\theta_{\rm col}=0.5$ mrad) we can calculate the bandwidth:

$$\frac{\Delta E_x}{E_x} = \sqrt{(2.77 \times 10^{-3})^2 + (9.90 \times 10^{-4})^2 + (6.57 \times 10^{-4})^2 + (1.95 \times 10^{-3})^2} = 0.36\%.$$

The dominant terms are the collimation term Eq. (24) and the emittance term Eq. (27); through correct design small bandwidth ICS sources can be built by minimizing these terms.

B. Bandwidth tuning

The bandwidth of an ICS light source is tunable and can be selected on the basis of user requirements, assuming both the electron and laser beams are round. Bandwidth selection is possible by selecting β^* at the IP and by setting the collimation angle, $\theta_{\rm col}$ that collects the scattered photons; these may for example comprise switchable, fixed-aperture collimators.

Typically the dominant terms that define the bandwidth of an inverse Compton source Eq. (23) are the collimation term Eq. (24) and the emittance term Eq. (27). The free parameter of the collimation term is the collimation angle $\theta_{\rm col}$, which can be adjusted either by changing the collimator aperture or changing its distance from the IP. Adjustable collimators have been designed for the ELI-NP-GBS γ -ray ICS source [23]; a similar design could be implemented at other ICS sources.

The emittance term is dependent both on the normalized transverse emittance ϵ_N and on β^* . It is more convenient to change the β -function at the IP with focusing rather than by varying the emittance, since the latter is dependent on the injector and collective effects prior to the IP. By using a larger β^* and a small collimator aperture, it is possible to reduce the contribution of the collimation and emittance terms so that they are negligible; thus the electron beam and laser pulse energy spread terms Eqs. (25) and (26) become dominant for accelerators with a sufficiently small emittance. This effectively places a lower limit on the bandwidth of an ICS source, i.e., it is limited by the energy spread of the electron beam $\Delta E_e/E_e$ and laser pulse $\Delta E_{\rm laser}/E_{\rm laser}$ as

$$\left(\frac{\Delta E_{\gamma}}{E_{\gamma}}\right)_{\min} \approx 2\frac{\Delta E_{e}}{E_{e}} + \frac{\Delta E_{\text{laser}}}{E_{\text{laser}}}.$$
 (28)

Consequently, any bandwidth above this limit can be achieved by an ICS source by tuning of the collimation angle and β^* so that a desired bandwidth, $\Delta E_{\gamma}/E_{\gamma}$, is achieved. Since the collimation and emittance terms are typically dominant, all other terms can be excluded and the solutions are bounded by

$$\frac{\Delta E_{\gamma}}{E_{\gamma}} > \sqrt{\left(\frac{\sigma_{\theta_{\text{col}}}}{E_{\theta_{\text{col}}}}\right)^2 + \left(\frac{\sigma_{\epsilon}}{E_{\epsilon}}\right)^2}.$$
 (29)

This results in myriad combinations of β^* and θ_{col} that satisfy a particular chosen bandwidth larger than this lower limit Eq. (28).

The different β^* , $\theta_{\rm col}$ combinations each give a different collimated flux; obviously we wish to choose the solution with the largest flux. The collimated flux \mathcal{F}_{Ψ} of each solution is calculated based on a method valid for small collimation angles ($\gamma\theta_{\rm col} < 1$) derived by Curatolo *et al.* [19]. Recast for our variable definitions, it becomes

$$\mathcal{F}_{\Psi} \propto \frac{(1+\sqrt[3]{X}\Psi^2/3)\Psi^2}{[1+(1+X/2)\Psi^2](1+\Psi^2)},$$
 (30)

where \mathcal{F} is the total (uncollimated) flux, $\Psi = \gamma \theta_{\rm col}$, and X is the recoil parameter. The solution giving the maximal flux is selected.

It is not practicable to calculate the flux from every combination of β^* and $\theta_{\rm col}$. Instead, an array of collimation angles $\theta_{\rm col}$ from 0 to $1/\gamma$ is used ($\gamma\theta_{\rm col} < 1$), and for a given bandwidth value the corresponding β^* is calculated using

$$\beta^* = \frac{2\gamma \epsilon_N}{1 + X} \frac{1}{\sqrt{\left(\frac{\Delta E_{\gamma}}{E_{\gamma}}\right)^2 - \left[\left(\frac{\sigma_{\theta_{\text{col}}}}{E_{\theta_{\text{col}}}}\right)^2 + \left(\frac{\sigma_{\epsilon}}{E_{e}}\right)^2 + \left(\frac{\sigma_{\text{laser}}}{E_{\text{laser}}}\right)^2\right]}}$$
(31)

which is a rearrangement of Eq. (23).

The collimated flux \mathcal{F}_{Ψ} is calculated for each combination produced via this method. The maximal collimated flux is selected and the combination of β^* and $\theta_{\rm col}$ corresponding to this solution is returned. This process can be applied to the case of a target bandwidth to determine $\theta_{\rm col}, \, \beta^*$, and collimated flux in the selected bandwidth. In addition, applying this method to a continuum of bandwidths allows us to map the possible operational settings of our ICS source, and to derive tuning curves such as the variation of the collimated flux with bandwidth.

C. ICS accelerator and laser considerations

In designing an ICS source a number of trade-offs are necessary due to the conflicting demands of electron beam dynamics and technical limitations. The incident photons will typically be obtained using a high-power optical cavity (cavity powers have been demonstrated in the 10–670 kW range [24]), which limits the repetition rate of the interaction below a few hundred MHz; as the cavity repetition rate increases the optical cavity path length must decrease, which amplifies the engineering challenges of the optical cavity such as sensitivity to misalignment errors, mirror heating, and so on. Here we assume the commonly used 1064 nm wavelength for the incident laser.

Taking these technical limitations into consideration, the electron bunches are preferably generated using a high repetition rate source with small emittance and energy spread. For a large flux, a smaller electron beam spot size at the IP is needed; while a larger spot can be beneficial for a narrower scattered photon bandwidth, this ultimately depends on the ϵ_N/β^* ratio. However, it is preferable that an ICS source is capable of adjusting the optics at the IP to maximize the flux into a chosen bandwidth, as described in the previous section.

Previous consideration has been given by several groups as to the appropriate accelerator technology for intense ICS photon production, and here we summarize some key points. Linear accelerators (linacs) and ERLs share the benefit of being able to utilize small photoinjector emittances, and the Cornell injector has demonstrated normalized values <1 mm-mrad for bunch charges up to at least 300 pC [25,26]. Linacs are, in practice, limited to repetition rates <10 kHz if using normal-conducting cavities, because of cavity heating limits. Superconducting linacs are limited perhaps to ~1 MHz if energy recovery is not employed [27]; this is because unrecovered high-energy beam dump power eventually becomes intolerable [28,29]. However, high-energy ERLs are now within reach due to the recent demonstration of multiturn acceleration and recovery at CBETA [7], allowing for multimilliampere operation.

When generating high energy photons, the operating power cost is significantly reduced with an ERL compared to a linac; a multiturn ERL has the added benefit of requiring less floor space and fewer SRF cavities. Consequently, a multiturn ERL with a high brightness, low energy spread electron beam at a high repetition rate is an ideal accelerator for an ICS source—CBETA is one such accelerator.

III. THE CBETA ACCELERATOR

A. Motivation for an energy-recovery linac

In the early days of high energy accelerators, two main categories existed: linear and circular; today, linacs and storage rings are both commonplace. As a generalization, electron linacs are typically capable of producing higher-quality beams (e.g., smaller emittance and bunch length) than storage rings. However, this comes with a lower energy efficiency than a storage ring; storage rings commonly produce average currents >10 mA that would be

impossible in a linac—the radio-frequency (rf) power cost and beam dump losses would be prohibitive [29].

ERLs combine the best of both types of accelerators; they can typically deliver higher-quality beams than those in storage rings, with greater energy efficiency than a linac [30]. In a typical one-turn ERL, a low energy beam is injected into a string of SRF cavities which accelerate the beam; the beam is then transported back to the cavity string where it is decelerated before being transported to a beam stop. The electrons' kinetic energy is returned to the rf field of the cavities and is used to accelerate following bunches; this allows for the beam power in the ERL to greatly exceed the available rf power.

As the beam parameters necessary for scientific research call for higher current and higher quality beams, ERLs are the accelerators best suited to meet this demand. Multiturn ERLs, which accelerate the electron beam multiple times before decelerating the beam, have the benefit of being able to reach higher energies without additional cost, power requirements, or floor space [29].

B. The Cornell-BNL ERL Test Accelerator

CBETA—the Cornell-BNL ERL Test Accelerator—is the first successful demonstration of an SRF multiturn ERL [7,31,32]; it features a nonscaling fixed-field alternating-gradient (FFA) arc constructed using permanent (Halbachtype) combined-function magnets [33], which transport the four beam energies (42, 78, 114, and 150 MeV) simultaneously in a common transport beam pipe [7,31,34]. CBETA is principally aimed at demonstrating the ERL technologies needed for a future electron-ion collider [31], but its parameters are also very attractive when considering hard x-ray photon production via ICS. CBETA comprises a 6 MeV injector, a single main linac cryomodule (MLC), splitter/recombiner sections (SX and RX), FFA arc (FA, TA, ZX, TB, FB), and beam stop; the layout of the four-turn configuration is shown in Fig. 2.

CBETA may be configured to operate using from one to four turns, with the corresponding top energies of each configuration being 42, 78, 114, and 150 MeV respectively; the design parameters are given in Table I. For a configuration of Y turns, the beam completes 2Y passes through the MLC, and 2Y - 1 passes through the FFA arc. The FFA arc can be divided into five sections: the arc sections (FA, FB) consist of FFA arc cells; the straight section (ZX) consists of FFA straight cells; and the transition sections (TA, TB) serve to match the beam between the arc and straight sections.

In the SX and RX sections, each beam energy passes through a different splitter/recombiner; this gives control of the Twiss parameters, horizontal dispersion and its derivative, R_{56} , and orbit; path length is varied using moving stages. The SX/RX lines are numbered one to four (S1, S2, etc.) corresponding to increasing beam energy, with the lowest-energy lines (S1/R1) on the inside and successive higher-energy lines further out. Each line simultaneously transports

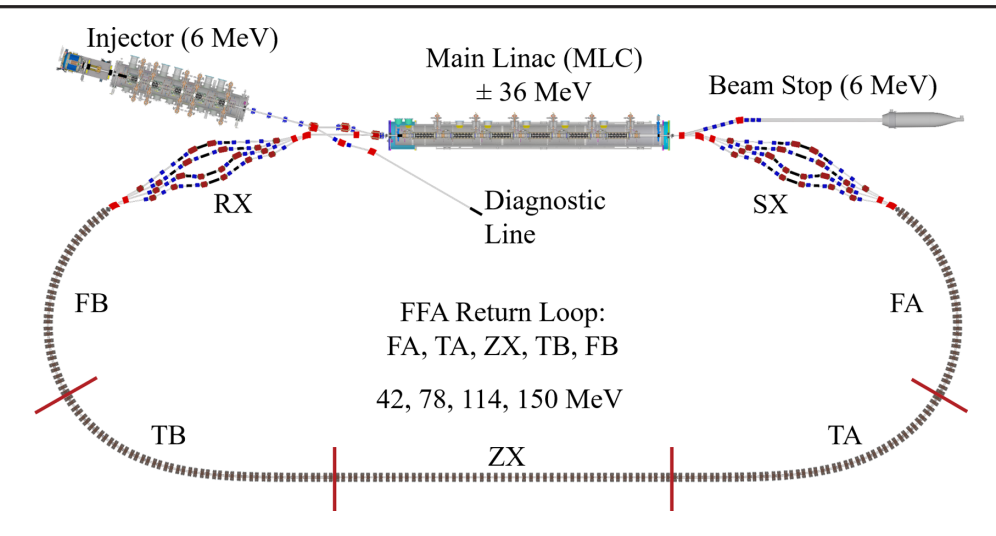


FIG. 2. Overview of the CBETA accelerator; a single FFA common transport arc (that includes the straight FFA section ZX) carries all four beam energies (42, 78, 114, and 150 MeV) within a single beam pipe. Matching of the entrance and exit beams at each energy is obtained through the SX and RX sections.

two beams—an accelerated pass and a decelerated pass—apart from at the highest-energy pass. Consequently, the beam optics of the accelerating and decelerating passes in the splitter lines are inherently coupled [31].

TABLE I. Key design parameters of CBETA.

Parameter	Quantity	Units
Kinetic energy	42, 78, 114, and 150	MeV
rf frequency	1.3	GHz
Bunch charge	≤2	nC
Repetition rate	1.3/N (integer N)	GHz
Maximum current	100 (one-turn), 40 (four-turn)	mA

Four passes have recently been experimentally demonstrated, with details given by Bartnik *et al.* [7]; this confirms that an ERL may deliver the beam parameters discussed in this paper.

IV. INVERSE COMPTON PRODUCTION AT CBETA

A. Electron and laser beam properties

The baseline electron beam parameters at the IP for the CBETA ICS were chosen based on the desire for an electron beam of high brightness and low energy spread for each of the four possible energies, assuming the same β^*

TABLE II. Electron beam parameters envisaged at the CBETA ICS interaction point (IP). The given baseline parameters—which assume the same β^* at the IP—allow a comparison of flux and bandwidth at different energies. The optimized values beneath those are where we have maximized the flux into a 0.5% scattered photon bandwidth through a suitable combination of beam spot size and collimation angle.

Parameter	Quantity				Unit
Turn number	1	2	3	4	
Electron kinetic energy, E_e	42	78	114	150	MeV
Repetition rate, f	162.5				MHz
Bunch charge, eN_e	32				pC
Transverse normalized rms emittance, ϵ_N	0.3				mm-mrad
rms bunch length, $\Delta \tau$	1.0 (3.33)				mm (ps)
Relative energy spread		5.0	0×10^{-4}		
		Baselin	e parameters		
β^* (at the IP)	1				cm
Electron bunch spot size, $\sigma_{\rm electron}$	6.01	4.42	3.65	3.19	μm
	Optimized for 0.5% bandwidth				
β^* (at the IP)	3.56	6.58	9.60	12.62	cm
Electron bunch spot size, σ_{electron}	11.34	11.34	11.34	11.34	μ m
Collimation angle, $\theta_{\rm col}$	1.533	0.830	0.569	0.433	mrad

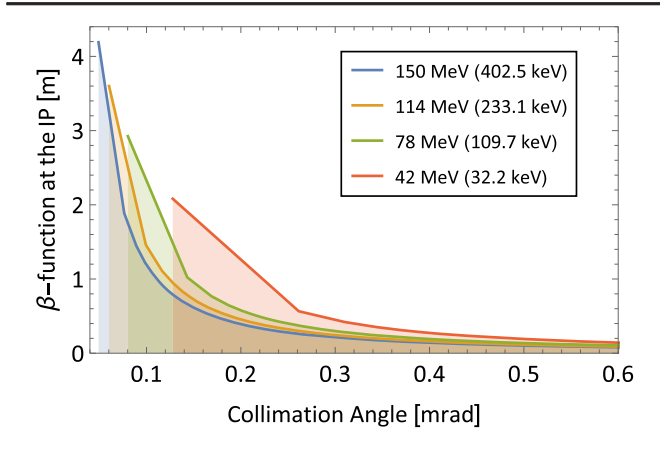


FIG. 3. Tuning curves of β^* against $\theta_{\rm col}$ for each of the nominal CBETA electron beam energies satisfying the maximal flux across the 0%–1% bandwidth range. The shaded area is the parameter space, while the line corresponds to the maximal flux solution for a given bandwidth. Minimized bandwidth solutions in this range have large β -functions at the IP and small collimation angles $\theta_{\rm col}$; the maximal bandwidth solutions have small β -functions and larger collimation angles $\theta_{\rm col}$.

at the IP; these values are given in the top section of Table II. Following the method outlined in Sec. II B, we have calculated the tuning curve of β^* as a function of $\theta_{\rm col}$ for maximal flux in a 0%–1% bandwidth, shown in Fig. 3. The tuning curve of collimated flux as a function of bandwidth is shown in Fig. 4. Electron beam parameters are quoted for narrow-band operation (0.5% bandwidth) in Table II by applying the optimization approach in Sec. II B, configured for a single bandwidth point.

While the design of CBETA allows for a maximum current nearly 8 times greater than the beam current assumed here, the coherent synchrotron radiation (CSR)

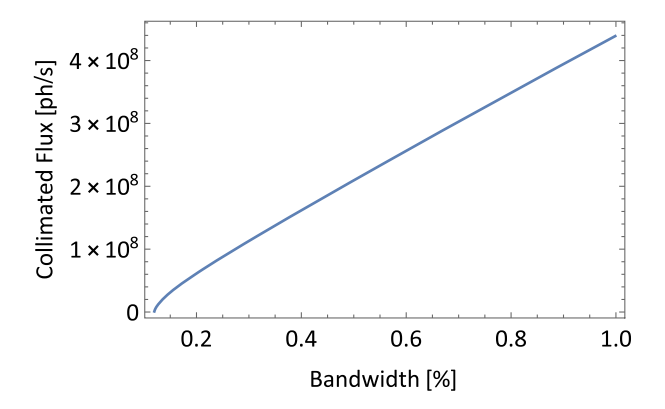


FIG. 4. Tuning curve of collimated flux against bandwidth for a 0%-1% bandwidth range, produced by tuning β^* and $\theta_{\rm col}$. The tuning curve is independent of beam energy for scattering scenarios within the Thomson regime, hence this tuning curve applies to all energies in CBETA. The left end of the tuning curve indicates the minimum possible bandwidth of the ICS source, which in CBETA is $\simeq 0.1\%$ and is determined by the electron beam energy spread.

TABLE III. Laser pulse parameters at the IP.

Parameter	Quantity	Unit
Wavelength, λ_{laser}	1064	nm
Photon energy, E_{laser}	1.17	eV
Pulse energy	62	μJ
Number of photons, N _{laser}	3.3×10^{14}	
Repetition rate, f	162.5	MHz
Spot size at the IP, σ_{laser}	25	μ m
Crossing angle, ϕ	5	deg
Pulse length	10	ps
Relative energy spread, $\Delta E_{\text{laser}}/E_{\text{laser}}$	6.57×10^{-4}	

disruption of the beam necessitates the lower bunch charge of 32 pC chosen [35]; the laser repetition rate cannot be increased due to the limitations on the repetition rate of the optical cavity providing the laser. The interaction laser is based on existing [18] and state-of-the-art [24] systems; the laser and optical cavity parameters are given in Table III. While a case can be made for a longer wavelength laser [36], the desire for higher energy x rays makes a Nd:YAG laser with a 1064 nm wavelength preferable for this design. Evaluating both the baseline and optimized ICS cases using Eqs. (18) and (22), the hourglass effect is negligible, while the angular crossing reduces the x-ray production by a factor of roughly 5, compared to the head-on collision $(\phi = 0)$; for our parameters, the angular crossing shortens the interaction time and suppresses the hourglass effect.

During the single turn commissioning of CBETA, the FFA was successfully tested with electron beams over an energy range from 39 to 59 MeV; we therefore consider that the ERL could be operated within this range to generate ICS photons. This would allow production of scattered photons with continuously tunable energy over the range 27.2 to 64.5 keV. Figure 5 indicates the possible scattered photon energies using either the fixed energies of the four passes, or from the variable electron energy using a single

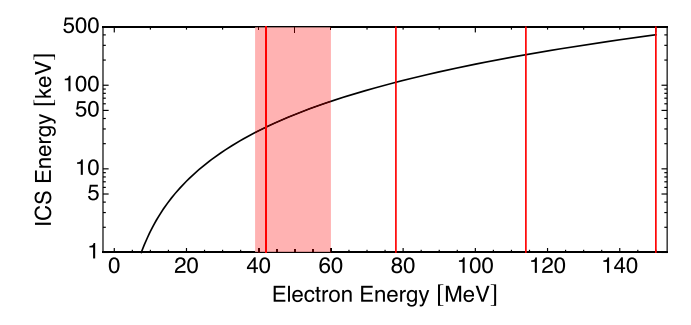


FIG. 5. An ICS source generating photons from each of the four CBETA ERL passes delivers the (fixed) scattered energies indicated here; we assume a fixed incident laser wavelength of 1064 nm. CBETA has also experimentally demonstrated tuning of single-pass acceleration from 39 to 59 MeV (indicated by the shaded region), which indicates the continuous tuning of scattered photon energy that an ERL in general might deliver.

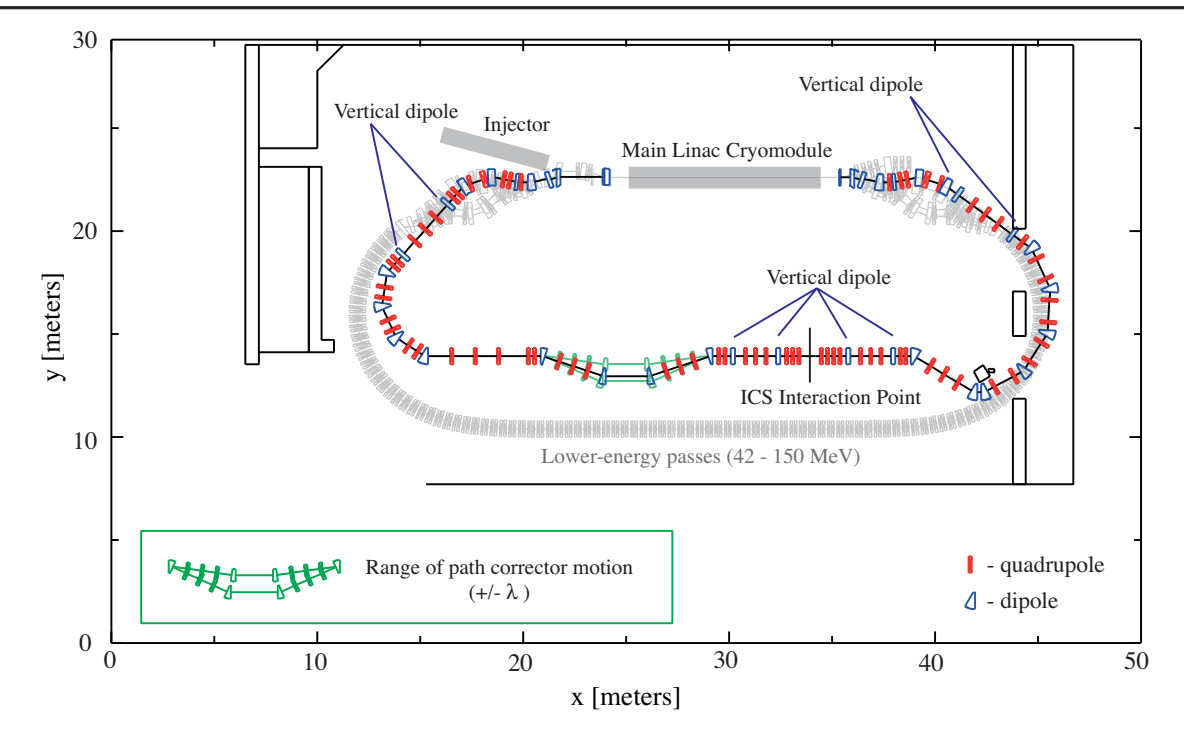


FIG. 6. Layout of the ICS bypass in CBETA; grayed beam line elements are already installed in the existing accelerator.

pass. Since tuning of the scattered photon energy is likely to be done in practical ICS sources by varying the electron energy, this figure indicates the likely tuning range that is possible either at CBETA or (analogously) at higher-energy ERLs.

B. Interaction bypass lattice

To utilize CBETA as an inverse Compton scattering source, a bypass line is required that replaces the ordinary fourth pass due to the stringent space restrictions in the existing FFA system; this leaves no space to arrange IP focusing nor for the laser recirculation cavity. The scattered photons from the ICS must also be produced in a different plane to the existing accelerator; the photons must be safely extracted from the footprint of the ERL since there is no space for an experimental hutch within the existing CBETA hall. The layout of such a bypass line is shown in Fig. 6. The bypass is configured for 150 MeV four-turn operation but could be adapted to operate with all nominal energies. The bypass was designed and optimized using the BMAD accelerator simulation library [37] and the TAO program [38] for simulating high energy particle beams in accelerators.

The bypass line diverts the 150 MeV electron beam after the fourth linac pass in the corresponding S4 splitter line; the electron beam then reenters the existing layout in the R4 line. The bypass replaces the FFA return loop, S4, from the fourth dipole onward and R4 up to the fourth dipole. The bypass will be located above the existing permanent magnet arc as the FFA arc is still used to transport the lower energy (42, 78, and 114 MeV) beams before and after the bypass.

A system of vertical doglegs, replacing sections of the S4 and R4 lines, are required to provide a 30 cm vertical elevation of the bypass line relative to the plane of the FFA return loop in order to avoid the existing accelerator. Bypass arc sections replace the existing FFA arc sections (FA, FB). Following the first arc, there is a horizontal dogleg used to close horizontal dispersion before the interaction region and offset the bypass from existing infrastructure.

At the interaction region (IR) the beam is again offset upward locally by a further 20 cm—to a 50 cm total offset above the FFA reference orbit height—using a pair of vertical doglegs; these are here called the IR doglegs. The further vertical offset is imposed so the photons are produced in a different plane to both the bypass line and FFA return loop which is necessary for the extraction of the x-ray beam to an external experimental hutch and in order to avoid irradiation of the FFA permanent magnets. A flexible focusing section within the pair of IR doglegs is used to focus to the required beam waist. The final focus section is designed to enable both $\beta^* = 1$ cm for the baseline case and $\beta^* = 12.6$ cm for the 0.5% bandwidth case (see Table II). The final focus section is constructed from seven quadrupoles with the laser recirculation cavity placed between the fourth and fifth quadrupole. This scheme allows the photons to be extracted via the first dipole of the downstream IR dogleg, minimizing the number of magnets requiring modification for photon extraction.

Within the straight section of the bypass following the IR, a variable path length adjustment is implemented based on the moving chicane described by Owen *et al.* [39]; this 4-dipole focusing chicane uses two mechanically adjustable swing arms each incorporating a quadrupole triplet, and a central bellows. The chicane replicates the function of the S4/R4 splitter/recombiners to allow variation of both R_{56} and path length for reentry into the MLC. Path length adjustment is made by opening the swing arms whilst increasing the dipole strengths accordingly; over a change in path length of $\pm \lambda_{rf}$ the variation in Twiss values (after rematching) is moderate.

Optics tuning of the bypass is limited by the compact layout of CBETA, the conditions required for energy

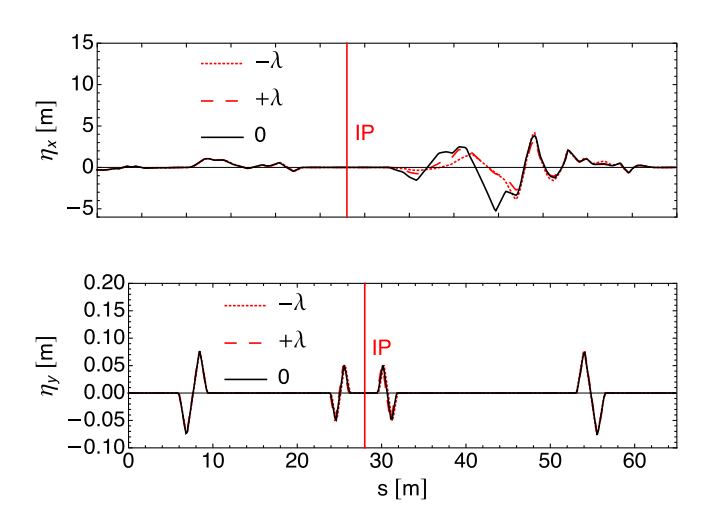


FIG. 7. Dispersion functions in the ICS bypass line for the 0.5% bandwidth case, showing the rematched conditions for different path length configurations $-\lambda_{RF}$, 0 and $+\lambda_{RF}$. The ICS interaction point (IP) is indicated.

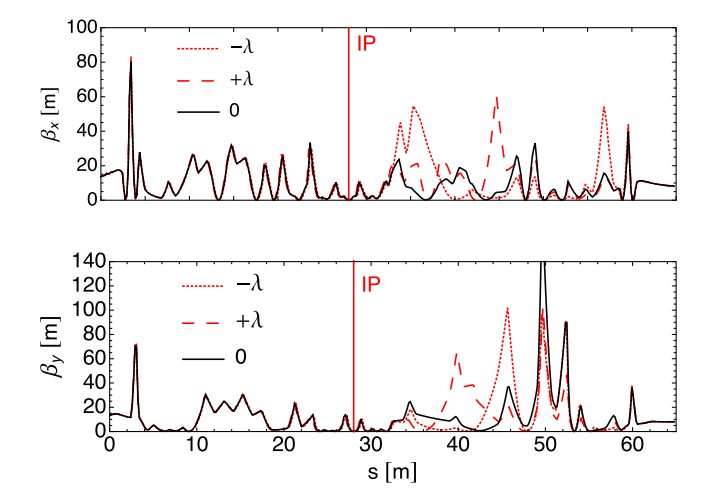


FIG. 8. Twiss functions in the ICS bypass line, showing the rematched conditions for different path length configurations $-\lambda_{\rm rf}$, 0 and $+\lambda_{\rm rf}$. The ICS interaction point (IP) is indicated.

recovery of the interacted beam ($R_{56} = 0$), and the necessity for the bypass to be constructed above the existing FFA return loop; the β -functions and dispersion are however still feasible. Plots of β -functions and dispersion in the bypass line for the 0.5% bandwidth case are shown in Figs. 7 and 8.

C. X-ray photon production and spectra

The predicted ICS production from CBETA has been calculated using the formulas derived in Sec. II, and is shown in Table IV. This table shows the optimized collimated flux for 0.5% bandwidth which has been produced using the analytical method described in Sec. II B. We see as expected that both the uncollimated and collimated fluxes are essentially independent of electron energy, which is typical of the ICS process. Using Eq. (7), we anticipate that the uncollimated fluxes of Table IV vary by only around 2% due to the small effects of varying the (baseline) electron beam sizes from 3 to 6 µm. A larger effect is from the 5 degree crossing angle; this crossing angle only causes a small (circa 1 keV) reduction in the Compton edge energy of the spectrum, but it reduces the effective time over which the incident laser photons may interact with the electrons by about a factor of 5. The anticipated spectrum is shown in Fig. 9, calculated by both ICCs3D [40] and ICARUS.

The code ICCs3D, a generalization of the ICCs code [14,40,41], computes radiation produced in ICS within the linear Compton regime (when $a_0 \ll 1$, and electron recoil is properly accounted for). In ICCs3D, a 3D laser pulse model replaces the 1D plane wave model used in ICCs. This modification is implemented in a manner described in Terzić et al. [40]; instead of all electrons experiencing the same laser field strength a_0 , as they do for a 1D plane wave, their effective laser field strength is dependent on the electron's distance from the laser's center at the moment of scattering. To calculate the anticipated spectral output, ICCs3D can use either the parameters of the electron beam or an arbitrary electron distribution, in addition to the laser parameters. For Fig. 9, a particle distribution was tracked by TAO through the bypass lattice to the IP; the distribution at the IP was provided to ICCs3D. When compared to the spectrum calculated using only the electron beam parameters, the differences were negligible.

ICARUS, the inverse Compton scattering semianalytic recoil-corrected ultrarelativistic spectrum code, uses a modified and corrected² version of the 2D formalism of Sun *et al.* [42]. ICARUS integrates the photons at small energy intervals that pass through a given 2D collimator aperture (here circular) for the fundamental laser mode.

²Note that there is an error in Eq. (53) of Sun's paper, where the prefactor gives that $dN/dE \propto L^2$ for a source-to-collimator distance L. Clearly, this should be $dN/dE \propto 1/L^2$; the other parts of the given equation are correct.

TABLE IV. Anticipated photon output for each of the four electron beam energies in CBETA, taking into account a 5 degree crossing angle. The uncollimated flux varies by around 2% due to the small effect of the electron spot size; X < 0.003 even at 150 MeV. The collimated flux has been optimized for a 0.5% bandwidth. The number of scattered photons is essentially independent of electron energy for a fixed electron spot size at the IP, and since both the Compton spectrum and the (relative) 0.5% bandwidth scale together with γ^2 , both the optimized spot size and the predicted collimated fluxes are the same at all electron energies.

	Electron kinetic energy (MeV)				
	42	78	114	150	Unit
X-ray peak energy	32.2	109.7	233.1	402.5	keV
Source size	5.84	4.35	3.62	3.17	$\mu\mathrm{m}$
Uncollimated flux	3.16×10^{10}	3.20×10^{10}	3.21×10^{10}	3.22×10^{10}	ph/s
Spectral density	9.82×10^{5}	2.92×10^{5}	1.38×10^{5}	8.00×10^{4}	ph/s eV
Average brilliance	9.23×10^{10}	3.19×10^{11}	6.81×10^{11}	1.18×10^{12}	ph/s mm ² mrad ² 0.1% bandwidth
Peak brilliance	2.80×10^{15}	1.00×10^{16}	2.18×10^{16}	3.80×10^{16}	ph/s mm ² mrad ² 0.1% bandwidth
		0.5% ba	ndwidth		
Source size	10.25	10.34	10.32	10.35	μ m
Collimated flux	2.09×10^{8}	2.09×10^{8}	2.09×10^{8}	2.09×10^{8}	ph/s 0.5% bandwidth

This code assumes that the electron bunch has a 3D Gaussian distribution, approximates the laser as a 3D Gaussian pulse, and is currently only valid for the head-on ($\phi = 0$) geometry; it has been validated against ICCS3D as well as the analytical results of this paper.

The spectral curves produced by both codes show good agreement with one another; once the angular crossing reduction factor, $R_{\rm AC}$, is applied, the integrated flux obtained from these curves agrees with Eq. (22), the collimated flux formula from Curatolo $et\ al.$ [19], and Eq. (10), Krafft and Priebe's approximation of the uncollimated flux into the 0.1% bandwidth at the Compton edge.

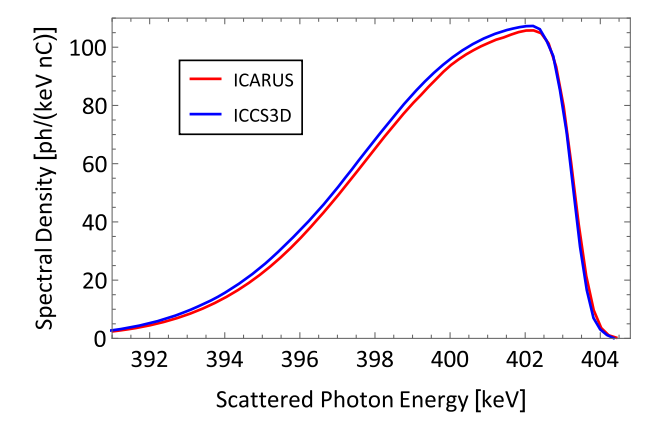


FIG. 9. Predicted spectral output (flux) from 1064 nm photons colliding head-on with the $E_e=150~\rm MeV$ (kinetic energy) electrons in CBETA; this spectrum was generated using the ICCS3D and ICARUS codes. This spectrum has a peak energy of 403.3 keV; using the proposed 5 degree crossing angle, the peak energy is reduced to 402.5 keV and the spectral density is reduced by a factor \sim 5.

V. DISCUSSION

A. Comparison with other radiation sources

Inverse Compton production of photons has the ability to extend the reach of monochromatic photon sources into the MeV range. Alternative sources are bremsstrahlung methods that generate intrinsically broad-spectrum radiation, line sources such as ¹³⁷Cs and ⁶⁰Co, and synchrotron radiation. Whilst line sources provide photons in the MeV scale, they are of course not tunable, emit isotropically and are difficult to handle (they cannot be turned off). Synchrotron radiation sources such as undulators are presently the primary method to generate intense, tunable radiation in the keV to MeV range.

It was already pointed out by Krafft and Priebe [12] that the flux and brilliance offered by ICS sources are not competitive at the photon energies produced by synchrotron radiation facilities; however, many of the recent ICS source designs are intended to compromise between typical laboratory-scale xray sources, such as rotating cathode tubes, and synchrotron radiation facilities in terms of size, cost, access, availability, and x-ray quality [20]. Table V contains measured or anticipated x-ray parameters from a number of other ICS sources. Though direct comparison is difficult as different designs have different objectives—one design may prioritize maximizing flux while another prioritizes having a narrower bandwidth—it is clear that most ICS sources are less than 200 keV and largely outperformed by synchrotron radiation facilities. However, some sources are capable of producing photon energies near or past the upper energy limit at most synchrotron radiation facilities.

The characteristic critical photon energy for SR is

$$\epsilon_c = \frac{3}{2} \frac{\hbar c \gamma^3}{\rho},\tag{32}$$

TABLE V. Comparison of existing and designed x-ray ICS sources.

ICS	Accelerator type	Scattered photon energy (keV)	Flux (ph/s)
cERL [18]	ERL	6.95	2.6×10^{7}
ALICE [43]	ERL	21.5	9×10^{5}
MIT ICS ^a [44]	Linac	3–30	3×10^{14}
MuCLS [45]	Storage ring	15–35	$0.443 - 1.78 \times 10^{10}$
Tsinghua [46]	Linac	51.7	1×10^{6}
ThomX ^a [47]	Storage ring	45–90	$1 \times 10^{10} - 10^{13}$
BriXS ^a [48,49]	ERL	20–180	$1 \times 10^{10} - 10^{13}$
CBETA ^a	ERL	32.2, 109.7, 233.1, 402.5	$3.16 - 3.21 \times 10^{10}$
NIJI-IV [50]	Storage ring	1200	3.1×10^{4}
$HI\gamma S^b$ [51]	Storage ring	1000-3000	$5 \times 10^7 - 5 \times 10^8$

^aDenotes design parameters for sources which are not yet demonstrated.

^bThe HIγS source is capable of scattered photon energies from 1–100 MeV with varying fluxes (see Table V of Ref. [51]). Shown is the lowest energy operational setting, most comparable to the source presented here.

which may be written as $\epsilon_c[\text{keV}] \simeq 0.665 E^2 B$ (for E given in GeV and B in tesla); this sets the scale for attainable photon energy. The highest-energy third-generation SR source today is SPRING-8 with E=8 GeV and $B\simeq 0.68$ T to obtain a critical energy $\epsilon_c\simeq 29$ keV for its broadband incoherent SR production; it is unlikely that a storage ring above 8 GeV will be built since rings such as SPRING-8 already have a physical circumference exceeding 1 km. The undulator output limit from a storage ring can be illustrated by setting the undulator K-parameter to be $K\sim 1$ and an undulator period $\lambda_u\sim 1$ cm. This gives a magnetic field limit of

$$B_0 = \frac{m_e c}{e} \frac{2\pi}{\lambda_u} K \sim 1 \text{ T.}$$
 (33)

The minimum undulator wavelength K = 0 possible (in the first harmonic of emission) is

$$\lambda_{\min} = \frac{\lambda}{2\gamma^2} \simeq 0.2 \text{ Å} \tag{34}$$

at 8 GeV ($\gamma \simeq 15,700$), which corresponds to a photon energy of 60 keV. In practice, most hard x-ray undulators and wigglers operate up to around 100 keV photon energy, with very few existing beam lines extending beyond that. Undulator output at higher harmonics is limited predominantly by the presence of magnetic phase errors, and the reduction in ideal flux from an rms phase error σ_{ϕ} can be modeled approximately [52] using the factor

$$R = \exp(-n^2 \sigma_{\phi}^2), \tag{35}$$

where n is the (odd) undulator harmonic, and σ_{ϕ} has typical values of a few degrees [53]. In practice this limits undulators to typically n < 15 in operation, although there is some discussion of whether rms error may be pessimistic

in some cases [54] and whether it may be reduced in future insertion devices [55,56].

We have surveyed the hard x-ray sources presently available at the high-energy storage rings APS [5], ESRF-EBS [4], PETRA-III [57], and SPRING-8 [6], using the codes SPECTRA [58] and SRW [59] to validate expected spectral output [60]. An example is the SPRING-8 BL10XU beam line, whose flux including an rms phase error of 5 degrees is shown in Fig. 10; this is compared with tabulated sample fluxes at the source points presented by SPRING-8 [6] and with the predicted flux from the CBETA ICS source design here.

The predicted brilliance of CBETA at the four operating energies is compared in Fig. 11 with a high-energy

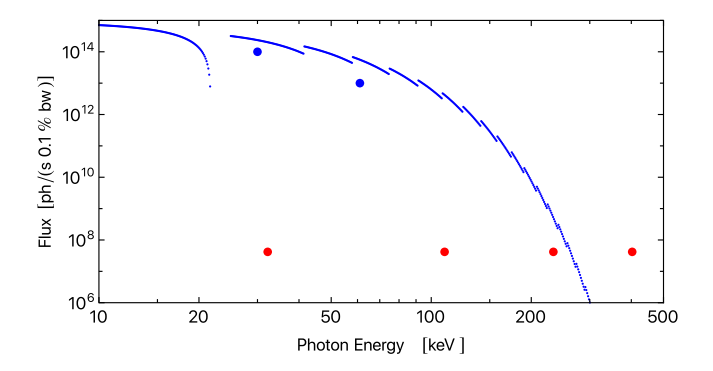


FIG. 10. Comparison of CBETA predicted flux (here flux in a 0.1% bandwidth to allow comparison with conventional calculations of undulator flux) at the four discrete operating energies given in Table IV with the output from a typical high-energy undulator. The undulator shown is the SPRING-8 BL10XU insertion device [6] assuming an rms phase error of 5 degrees. Whilst this undulator is not designed to deliver good output at high harmonic number, it offers a useful guide to possible third-generation source output in the 100 to 500 keV range. The measured flux at 30 and 61 keV for this beam line is also shown [6]. We predict that CBETA flux at 402 keV (150 MeV electron energy) exceeds that from third-generation sources.

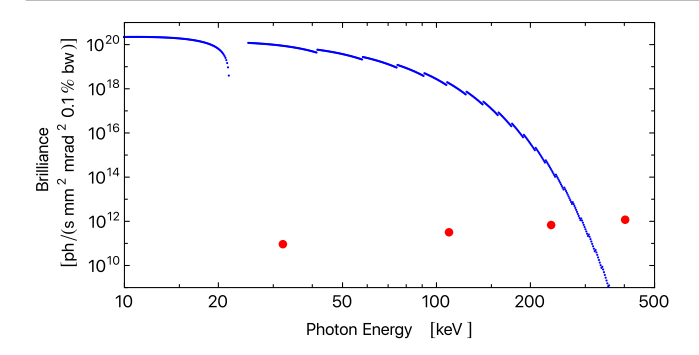


FIG. 11. Comparison of CBETA predicted brilliance at the four discrete operating energies given in Table IV with the output from a typical high-energy undulator. The undulator shown is the SPRING-8 BL10XU insertion device [6] assuming an rms phase error of 5 degrees. We predict that CBETA brilliance at 402 keV (150 MeV electron kinetic energy) exceeds that from third-generation sources.

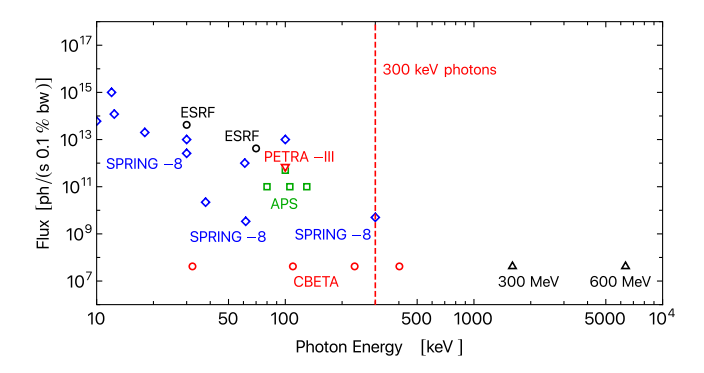


FIG. 12. On-sample measured fluxes from APS, ESRF-EBS, PETRA-III, and SPRING-8 for which information has been published [4–6,57]. This is compared with the predicted CBETA outputs at the four discrete photon energies from 32 to 402 keV, and the predicted flux obtained by scaling the CBETA electron energy to 300 MeV (1600 keV photons) and 600 MeV (6360 keV photons). Whilst third-generation sources are superior to ICS sources up to photon energies around 300 keV, they do not produce usable flux above 400 keV.

undulator (BL10XU) at the world's highest-energy third-generation synchrotron source, SPRING-8 [6]. This undulator is indicative of what is achievable from other undulators on these high-energy sources. We see as expected that storage ring sources produce greater brilliance even at high harmonic number for photon energies up to approximately 300 keV. However, the fundamental energy scaling of synchrotron radiation and the finite undulator magnetic field quality means that the ICS output from CBETA becomes superior in the 400 keV regime. This performance is mirrored in the predicted flux that is shown in Fig. 10, which makes the same assumption of a 5 degree rms phase error; the measured flux at 30 and 61 keV is superior to that possible from an ICS source, but at 400 keV this is reversed.

Figure 12 compares the on-sample measured fluxes from those high-energy synchrotron beam lines (>30 keV) for which data is available [4–6,57]. Almost no beam line generates output above 100 keV, and above 400 keV we have shown that ICS is in any case a superior source. Extending the demonstrated CBETA parameters to higher electron energy we would expect the collimated flux values to remain nearly constant; hence we may estimate the likely possible flux for MeV-scale photons from an ERL-based source. Two indicative electron energies (300 and 600 MeV) are also shown in Fig. 12.

B. Applications

The proposed CBETA ICS is a high-flux, small-bandwidth, quasimonochromatic source of x rays, producing high peak energy photons in the 100s keV range. The large flux opens up a parameter space for x-ray applications previously attainable only at the largest synchrotrons, and then only using substantial x-ray optics. We now outline some possible uses.

Important applications of such a source are x-ray absorption spectroscopy and x-ray fluorescence [61]. High-energy XRF is an application that is particularly well suited for this ICS source; due to collimation there is no need to monochromate, avoiding complex x-ray optical instrumentation. Energy-sensitive x-ray fluorescence detection can be provided by a solid-state detector coupled to a pulse-height analyzer. For example, in any analysis of a fission reactor's fuel rods, the $K\alpha$ and $K\beta$ lines for uranium $(K\alpha_1 = 98.4 \text{ keV}, K\beta_1 = 111.3 \text{ keV})$ and plutonium $(K\alpha_1 = 103.7 \text{ keV}, K\beta_1 = 117.2 \text{ keV})$ could be probed [62]. Quantitative assays would be performed by means of a low-Z reference scatterer to ascertain the spectral content of the broadband incident beam through elastic and Compton scattering into the same detector. The fluorescence efficiency of the detection scheme is then provided by the known photoabsorption cross sections of the elements of interest versus incident energy.

The deep penetrating power of a high-energy x-ray source provides the opportunity for imaging of thick specimens that would not be possible at lower energies. These range from straightforward techniques such as 2D shadowgraphy through to 3D reconstruction with tomography [63].

Another ready application exploits the high flux and high energy of the source: energy-dispersive x-ray diffraction (EDXRD) for the identification of constituents of a polycrystalline/powdered sample. A high-flux source would allow for rapid identification of the minerals in a mined ore sample, while the high energy of the source allows for the inspection of thick specimens. In EDXRD [64] one applies the nonmonochromated peak to a specimen of the material of interest, and checks for diffracted photons with an energy-sensitive solid-state detector. From the energy we deduce the wavelength, and applying the Bragg relation we

find the combination of Miller indices and lattice spacing of the reflecting crystalline planes. Checking for many such reflections in a particular mineral provides constituent identification; the intensity of these Bragg peaks provides the relative abundances of the various mineral components. Our source serves as a high flux alternative to SR facilities [65] which typically operate up to approximately 200 keV, though some facilities are capable of higher energy. Additionally, our design provides photons well beyond that energy range.

Turning to more ambitious but equally exciting applications, significant beam line infrastructure would be required here in contrast to the applications just discussed. In the first, we propose to perform nonresonant inelastic x-ray scattering (NIXS) in order to examine the dynamic electronic response of quantum materials throughout the periodic chart. The high incident photon energy and large flux provided by our source allows us to test exciting materials such as transition metal oxides, which are a test bed for theories such as the Mott-Hubbard model, since they provide fresh insight into the candidates for useful applications such as high-temperature superconductors [66,67]. The energy resolution requirements for this method are severe: 1 eV out of 100 keV; it would require the development of high-energy x-ray monochromator and analyzer optics, most likely through synthetic multilayers in order to provide an optimal match to beam optics. In our implementation of the NIXS technique the analyzers are arrayed at a range of scattering angles to provide a comprehensive set of momentum transfers. The pass energy of the analyzers is fixed while the incident energy is scanned to provide variable energy transfers with a double crystal monochromator configuration [68,69]. Because of sample self-absorption and the weak signal set by the small Thomson cross section [68], the reach of NIXS is especially limited for medium to large Z elements. Performance of NIXS at an incident energy of 100 keV as proposed here would provide an attenuation length due to photoabsorption of 100 microns [70]. This is a factor of 25 greater [71] than that provided at the contemporary hard NIXS facility at the Advanced Photon Source [69] which operates with an incident energy of 10 keV when performing spectroscopy at the low energy transfers of great interest in condensed matter studies.

In our second ambitious application of Compton-produced photons, a mixing crystal would be employed to generate entangled photon pairs via parametric down conversion (PDC). Here the efficiency is boosted by working at high input photon energy, since the intensity of the vacuum fluctuations present at the mixer's input varies as the fourth power of the operating energy [72]. Besides the accomplishment of achieving PDC at (about) a factor of 5 higher energy than is currently practiced [73], it will provide exciting applications, for example twin microscopy—which promises enhanced visibility through quantum ghost imaging

of otherwise inaccessible specimens—and twin ellipsometry for the careful examination of surface structures [74]. To compare PDC applications with contemporary SR sources: the ghost imaging demonstration of Schori *et al.* [73] was recently performed with an input energy of 22.3 keV. Using our source at 100 keV would provide PDC generation according to the aforementioned scaling law with a zero point energy flux advantage of about 400 times greater.

The final ambitious application, nuclear resonance fluorescence (NRF), is a technique suitable for a future, higherenergy ERL-based ICS, with an electron beam energy on the order of 350 MeV or above. This electron beam energy regime boosts the Compton backscattered photons into the regime of gamma rays with an energy of 2.2 MeV or above. These in turn would be used to excite nuclear levels identifying them with an energy sensitive solid state detector, achieving the nuclear sister spectroscopy to the atomic fluorescence spectroscopy mentioned in our first application. Such spectroscopy would be very useful in assaying nuclear materials, for example identification of manufacturing defects in fission fuel assemblies, nonproliferation security of spent fission fuel, and identification of unknown legacy wastes [75–79]. Moving up to photon energies above 5 MeV (requiring a GeV-scale electron ERL) would open up the nuclear transmutation reactions $(\gamma, p), (\gamma, n), (\gamma, f)$ with potentially far-reaching applications in waste transmutation [80], the understanding of fission dynamics [81-83], and bespoke medical isotope production from existing waste streams [84].

VI. CONCLUSION

In this paper we have shown a method of adapting an existing multiturn energy-recovery linac to produce a quasimonochromatic source of photons in the 100s keV range with higher flux and spectral density than hitherto achieved. We establish that such a source is highly desired for a range of scientific and industrial applications that are not yet fully served by existing sources. A specific design of electron transport beam line for the CBETA energy recovery linac is presented which is compatible with the existing accelerator and enables inverse Compton scattering for photon production. The expected output properties are calculated and compared to monochromated photons of the same energy generated by much larger storage-ring-based facilities, thereby demonstrating the competitiveness of this approach.

ACKNOWLEDGMENTS

This work was supported by NSF Grant No. DMR-0807731 and DOE Award No. DE-SC0012704, and in part by the Science and Technology Facilities Council under Grants No. ST/G008248/1 and No. ST/S505523/1. B. T. gratefully acknowledges the support of U.S. National Science Foundation CAREER Grant No. 1847771. G. K.

was supported at Jefferson Lab by U.S. DOE Contract No. DE-AC05-06OR23177. We would like to thank Stanislav Stoupin for useful discussions.

- [1] J. Als-Nielsen and D. McMorrow, *Elements of Modern X-ray Physics* (Wiley, New York, 2011).
- [2] U. Kneissl, H. Pitz, and A. Zilges, Investigation of nuclear structure by resonance fluorescence scattering, Prog. Part. Nucl. Phys. 37, 349 (1996).
- [3] R. Hajima et al., Application of laser Compton scattered gamma-ray beams to nondestructive detection and assay of nuclear material, Eur. Phys. J. Special Topics 223, 1229 (2014).
- [4] ESRF-EBS beam line list, https://www.esrf.eu/home/ UsersAndScience/Accelerators/ebs---extremely-brilliantsource/ebs-parameters.html.
- [5] APS beam line list, https://www.aps.anl.gov/Beamlines/ Directory.
- [6] SPRING-8 beam line list, http://www.spring8.or.jp/en/ about us/whats sp8/facilities/bl/list/.
- [7] A. Bartnik *et al.*, CBETA: First Multipass Superconducting Linear Accelerator with Energy Recovery, Phys. Rev. Lett. 125, 044803 (2020).
- [8] E. Feenberg and H. Primakoff, Interaction of cosmic-ray primaries with sunlight and starlight, Phys. Rev. 73, 449 (1948).
- [9] R. H. Milburn, Electron Scattering by an Intense Polarized Photon Field, Phys. Rev. Lett. **10**, 75 (1963).
- [10] F. Arutyunian and V. Tumanian, The Compton effect on relativistic electrons and the possibility of obtaining high energy beams, Phys. Lett. 4, 176 (1963).
- [11] C. Bemporad, R. H. Milburn, N. Tanaka, and M. Fotino, High-energy photons from Compton scattering of light on 6.0-GeV electrons, Phys. Rev. 138, B1546 (1965).
- [12] G. A. Krafft and G. Priebe, Compton sources of electromagnetic radiation, Rev. Accel. Sci. Techol. 03, 147 (2010).
- [13] C. Sun, J. Li, G. Rusev, A. Tonchev, and Y. Wu, Energy and energy spread measurements of an electron beam by Compton scattering method, Phys. Rev. ST Accel. Beams 12, 062801 (2009).
- [14] N. Ranjan, B. Terzić, G. Krafft, V. Petrillo, I. Drebot, and L. Serafini, Simulation of inverse Compton scattering and its implications on the scattered linewidth, Phys. Rev. Accel. Beams 21, 030701 (2018).
- [15] R. Hajima and M. Fujiwara, Narrow-band GeV photons generated from an x-ray free-electron laser oscillator, Phys. Rev. Accel. Beams **19**, 020702 (2016).
- [16] T. Suzuki, General formulas of luminosity for various types of colliding beam machines, Technical Report, National Laboratory for High Energy Physics, 1976, https:// inspirehep.net/files/56200f5110f34e07afe6e25af9f95528.
- [17] V. B. Berestetskii, L. P. Pitaevskii, and E. M. Lifshitz, Quantum Electrodynamics (Pergamon, New York, 1982), Vol. 4.
- [18] T. Akagi, A. Kosuge, S. Araki, R. Hajima, Y. Honda, T. Miyajima, M. Mori, R. Nagai, N. Nakamura, M. Shimada, T. Shizuma, N. Terunuma, and J. Urakawa, Narrow-band

- photon beam via laser Compton scattering in an energy recovery linac, Phys. Rev. Accel. Beams **19**, 114701 (2016)
- [19] C. Curatolo, I. Drebot, V. Petrillo, and L. Serafini, Analytical description of photon beam phase spaces in inverse Compton scattering sources, Phys. Rev. Accel. Beams 20, 080701 (2017).
- [20] K. E. Deitrick, G. A. Krafft, B. Terzić, and J. R. Delayen, High-brilliance, high-flux compact inverse Compton light source, Phys. Rev. Accel. Beams 21, 080703 (2018).
- [21] F. Hartemann, W. Brown, D. Gibson, S. Anderson, A. Tremaine, P. Springer, A. J. Wootton, E. Hartouni, and C. Barty, High-energy scaling of Compton scattering light sources, Phys. Rev. ST Accel. Beams 8, 100702 (2005).
- [22] Y. Miyahara, Luminosity of angled collision of strongly focused beams with different Gaussian distributions, Nucl. Instrum. Methods Phys. Res., Sect. A 588, 323 (2008).
- [23] G. Paternò, P. Cardarelli, M. Marziani, E. Bagli, F. Evangelisti, M. Andreotti, M. Gambaccini, V. Petrillo, I. Drebot, A. Bacci *et al.*, A collimation system for eli-np gamma beam system—Design and simulation of performance, Nucl. Instrum. Methods Phys. Res., Sect. B 402, 349 (2017).
- [24] H. Carstens, N. Lilienfein, S. Holzberger, C. Jocher, T. Eidam, J. Limpert, A. Tünnermann, J. Weitenberg, D. C. Yost, A. Alghamdi *et al.*, Megawatt-scale average-power ultrashort pulses in an enhancement cavity, Opt. Lett. 39, 2595 (2014).
- [25] C. Gulliford, A. Bartnik, I. Bazarov, L. Cultrera, J. Dobbins, B. Dunham, F. Gonzalez, S. Karkare, H. Lee, H. Li, Y. Li, X. Liu, J. Maxson, C. Nguyen, K. Smolenski, and Z. Zhao, Demonstration of low emittance in the Cornell energy recovery linac injector prototype, Phys. Rev. ST Accel. Beams 16, 073401 (2013).
- [26] A. Bartnik, C. Gulliford, I. Bazarov, L. Cultera, and B. Dunham, Operational experience with nanocoulomb bunch charges in the Cornell photoinjector, Phys. Rev. ST Accel. Beams 18, 083401 (2015).
- [27] J. Stohr, Linac coherent light source II (LCLS-II) conceptual design report, Report No. SLAC-R-978, https://www.slac.stanford.edu/pubs/slacreports/reports19/slac-r-978.pdf.
- [28] S. M. Gruner, D. Bilderback, I. Bazarov, K. Finkelstein, G. Krafft, L. Merminga, H. Padamsee, Q. Shen, C. Sinclair, and M. Tigner, Energy recovery linacs as synchrotron radiation sources (invited), Rev. Sci. Instrum. 73, 1402 (2002).
- [29] L. Merminga, D. R. Douglas, and G. A. Krafft, High-current energy-recovering electron linacs, Annu. Rev. Nucl. Part. Sci. **53**, 387 (2003).
- [30] G. Hoffstaetter, V. Litvinenko, and H. L. Owen, Nucl. Instrum. Methods Phys. Res., Sect. A 557, 345 (2006).
- [31] G. Hoffstaetter, D. Trbojevic, and C. Mayes, CBETA design report, cornell-BNL ERL test accelerator, arXiv:1706.04245.
- [32] C. Gulliford, N. Banerjee, A. Bartnik, J. Crittenden, K. Deitrick, J. Dobbins, G. H. Hoffstaetter, P. Quigley, K. Smolenski, J. S. Berg, R. Michnoff, S. Peggs, and D. Trbojevic, Measurement of the per cavity energy recovery efficiency in the single turn Cornell-Brookhaven ERL test

- accelerator configuration, Phys. Rev. Accel. Beams 24, 010101 (2021).
- [33] S. Brooks, G. Mahler, J. Cintorino, J. Tuozzolo, and R. Michnoff, Permanent magnets for the return loop of the Cornell-Brookhaven energy recovery linac test accelerator, Phys. Rev. Accel. Beams 23, 112401 (2020).
- [34] N. Tsoupas, J. S. Berg, S. Brooks, J. Crittenden, G. Mahler, F. Mot, V. Ptitsyn, D. Trbojevic, and S. Tygier, The beam optics of the FFAG cell of the CBETA ERL accelerator, in Proceedings of the 8th International Particle Accelerator Conference (IPAC 2017): Copenhagen, Denmark, 2017 (JACoW, Geneva, Switzerland, 2017), MOPIK122, https:// doi.org/10.18429/JACoW-IPAC2017-MOPIK122.
- [35] W. Lou and G. H. Hoffstaetter, Coherent synchrotron radiation wake expressions with two bending magnets and simulation results for a multiturn energy-recovery linac, Phys. Rev. Accel. Beams 23, 054404 (2020).
- [36] I. V. Pogorelsky, M. Polyanskiy, and T. Shaftan, Converting conventional electron accelerators to high peak brilliance Compton light sources, Phys. Rev. Accel. Beams 23, 120702 (2020).
- [37] D. Sagan, The Bmad Manual, https://www.classe.cornell.edu/bmad/manual.html.
- [38] D. Sagan, The Tao Manual, https://www.classe.cornell.edu/bmad/tao.html.
- [39] H. L. Owen and P. H. Williams, A modular path length corrector for recirculating linacs, Nucl. Instrum. Methods Phys. Res., Sect. A 662, 12 (2012).
- [40] B. Terzić, A. Brown, I. Drebot, T. Hagerman, E. Johnson, G. A. Krafft, C. Maroli, V. Petrillo, and M. Ruijter, Improving performance of inverse Compton sources through laser chirping, Europhys. Lett. 126, 12003 (2019).
- [41] G. Krafft, E. Johnson, K. Deitrick, B. Terzić, R. Kelmar, T. Hodges, W. Melnitchouk, and J. Delayen, Laser pulsing in linear Compton scattering, Phys. Rev. Accel. Beams 19, 121302 (2016).
- [42] C. Sun and Y. K. Wu, Theoretical and simulation studies of characteristics of a Compton light source, Phys. Rev. ST Accel. Beams 14, 044701 (2011).
- [43] G. Priebe, D. Laundy, P. Phillips, D. Graham, S. Jamison, S. Vassilev, E. Seddon, J. Rosenzweig, G. Krafft, T. Heinzl et al., First results from the Daresbury Compton backscattering x-ray source (cobald), in Hard X-Ray, Gamma-Ray, and Neutron Detector Physics XII (International Society for Optics and Photonics (2010), Vol. 7805, p. 780513, https://doi.org/10.1117/12.859671.
- [44] W. S. Graves *et al.*, Compact x-ray source based on burst-mode inverse Compton scattering at 100 kHz, Phys. Rev. ST Accel. Beams **17**, 120701 (2014).
- [45] E. Eggl, M. Dierolf, K. Achterhold, C. Jud, B. Günther, E. Braig, B. Gleich, and F. Pfeiffer, The Munich compact light source: Initial performance measures, J. Synchrotron Radiat. 23, 1137 (2016).
- [46] Y. Du, L. Yan, J. Hua, Q. Du, Z. Zhang, R. Li, H. Qian, W. Huang, H. Chen, and C. Tang, Generation of first hard x-ray pulse at Tsinghua Thomson scattering x-ray source, Rev. Sci. Instrum. 84, 053301 (2013).
- [47] K. Dupraz, M. Alkadi, M. Alves, L. Amoudry, D. Auguste, J.-L. Babigeon, M. Baltazar, A. Benoit, J. Bonis,

- J. Bonenfant *et al.*, The ThomX ICS source, Phys. Open 5, 100051 (2020).
- [48] P. Cardarelli, A. Bacci, R. Calandrino, F. Canella, R. Castriconi, S. Cialdi, A. Del Vecchio, F. di Franco, I. Drebot, M. Gambaccini *et al.*, BriXS, a new x-ray inverse Compton source for medical applications, Phys. Med. 77, 127 (2020).
- [49] I. Drebot *et al.*, Status of compact inverse Compton sources in Italy: BriXS and STAR, Proc. SPIE Int. Soc. Opt. Eng. **11110**, 14 (2019).
- [50] N. Sei, H. Ogawa, and S. Okuda, Demonstration of narrow-band x-ray beam by inverse Compton scattering with stored spontaneous emission, J. Appl. Phys. **121**, 023103 (2017).
- [51] H. R. Weller, M. W. Ahmed, H. Gao, W. Tornow, Y. K. Wu, M. Gai, and R. Miskimen, Research opportunities at the upgraded HIγS facility, Prog. Part. Nucl. Phys. 62, 257 (2009).
- [52] R. Walker, Interference effects in undulator and wiggler radiation sources, Nucl. Instrum. Methods Phys. Res., Sect. A 335, 328 (1993).
- [53] R. P. Walker, Phase errors and their effect on undulator radiation properties, Phys. Rev. ST Accel. Beams 16, 010704 (2013).
- [54] T. Tanaka, Universal representation of undulator phase errors, Phys. Rev. Accel. Beams 21, 110704 (2018).
- [55] C. S. Hwang, J. C. Jan, C. S. Chang, S. D. Chen, C. H. Chang, and T. M. Uen, Development trends for insertion devices of future synchrotron light sources, Phys. Rev. ST Accel. Beams 14, 044801 (2011).
- [56] J.-C. Huang, H. Kitamura, C.-K. Yang, C.-H. Chang, C.-H. Chang, and C.-S. Hwang, Challenges of in-vacuum and cryogenic permanent magnet undulator technologies, Phys. Rev. Accel. Beams 20, 064801 (2017).
- [57] PETRA III Beam Line List, https://photon-science.desy.de/ facilities/petra_iii/beamlines/index_eng.html.
- [58] T. Tanaka and H. Kitamura, SPECTRA: A synchrotron radiation calculation code, J. Synchrotron Radiat. 8, 1221 (2001).
- [59] O. Chubar, A. Fluerasu, L. Berman, K. Kaznatcheev, and L. Wiegart, Wavefront propagation simulations for beam lines and experiments with "synchrotron radiation workshop", J. Phys. Conf. Ser. 425, 162001 (2013).
- [60] T. Tanaka, T. Seike, X. Marchal, T. Bizen, T. Hara, and H. Kitamura, Field measurement and correction of the very long in-vacuum x-ray undulator at the SPring-8, Nucl. Instrum. Methods Phys. Res., Sect. A 467–468, 149 (2001).
- [61] P. Willmott, An Introduction to Synchrotron Radiation: Techniques and Applications (John Wiley & Sons, New York, 2019), Chapter on spectroscopic techniques.
- [62] G. J. Havrilla, V. Lopez, K. McIntosh, W. Elam, and D. Robinson, Feasibility of uranium detection through container walls using ultrahigh-energy x-ray fluorescence, Microscopy Today 23, 30 (2015).
- [63] J. Als-Nielsen and D. McMorrow, *Elements of Modern X-Ray Physics* (Wiley, New York, 2011), Chap. 9.
- [64] B. Kämpfe, F. Luczak, and B. Michel, Energy dispersive x-ray diffraction, Particle Particle Syst. Characterization **22**, 391 (2005).

- [65] Structural Materials Beam Line, https://www.chess.cornell.edu/structural-materials-beamline.
- [66] M. Hasan, P. Montano, E. Isaacs, Z.-X. Shen, H. Eisaki, S. Sinha, Z. Islam, N. Motoyama, and S. Uchida, Momentum-resolved charge excitations in a prototype one-dimensional Mott insulator, Phys. Rev. Lett. 88, 177403 (2002).
- [67] E. Isaacs and P. Platzman, Inelastic x-ray scattering in condensed matter physics, Phys. Today 49, No. 2, 40 (1996).
- [68] W. Schülke, Electron Dynamics by Inelastic X-Ray Scattering (Oxford University Press, New York, 2007), Chaps. 2 and 3.
- [69] T. Fister, G. Seidler, L. Wharton, A. Battle, T. Ellis, J. Cross, A. Macrander, W. Elam, T. Tyson, and Q. Qian, Multielement spectrometer for efficient measurement of the momentum transfer dependence of inelastic x-ray scattering, Rev. Sci. Instrum. 77, 063901 (2006).
- [70] Transmitted Intensity and Linear Attenuation Coefficient, https://www.nde-ed.org/EducationResources/ CommunityCollege/Radiography/Physics/attenuationCoef .htm.
- [71] Tungsten, https://physics.nist.gov/PhysRefData/XrayMassCoef/ ElemTab/z74.html.
- [72] P. Eisenberger and S. McCall, X-ray Parametric Conversion, Phys. Rev. Lett. 26, 684 (1971).
- [73] A. Schori, D. Borodin, K. Tamasaku, and S. Shwartz, Ghost imaging with paired x-ray photons, Phys. Rev. A 97, 063804 (2018).
- [74] D. S. Simon, G. Jaeger, and A. V. Sergienko, *Quantum Metrology, Imaging, and Communication* (Springer, New York, 2017), Chaps. 4 and 7.
- [75] D. Angal-Kalinin *et al.*, PERLE. Powerful energy recovery linac for experiments. Conceptual design report, J. Phys. G 45, 065003 (2018).
- [76] C. Angell, R. Hajima, T. Hayakawa, T. Shizuma, H. Karwowski, and J. Silano, Demonstration of a transmission nuclear resonance fluorescence measurement for a realistic radioactive waste canister scenario, Nucl. Instrum. Methods Phys. Res., Sect. B 347, 11 (2015).

- [77] A. M. Bolind and M. Seya, The state of the art of the nondestructive assay of spent nuclear fuel assemblies— A critical review of the spent fuel NDA project of the U.S. Department of Energy's next generation safeguards initiative (2015), https://doi.org/10.11484/jaea-review-2015-027.
- [78] C. Geddes, B. Ludewigt, J. Valentine, B. Quiter, M.-A. Descalle, G. Warren, M. Kinlaw, S. Thompson, D. Chichester, C. Miller, and S. Pozzi, Impact of monoenergetic photon sources on nonproliferation applications final report (2017), https://www.osti.gov/biblio/1376659.
- [79] E. Kwan, G. Rusev, A. S. Adekola, F. Dönau, S. L. Hammond, C. R. Howell, H. J. Karwowski, J. H. Kelley, R. S. Pedroni, R. Raut, A. P. Tonchev, and W. Tornow, Discrete deexcitations in U-235 below 3 MeV from nuclear resonance fluorescence, Phys. Rev. C 83, 041601 (2011).
- [80] H. u. Rehman, J. Lee, and Y. Kim, Optimization of the laser-Compton scattering spectrum for the transmutation of high-toxicity and long-living nuclear waste, Ann. Nucl. Energy 105, 150 (2017).
- [81] G. Bellia, A. Zoppo, C. Maiolino, E. Migneco, and G. Russo, Towards a better understanding of deep subthreshold photofission of 238U, Z. Phys. A **314**, 43 (1983).
- [82] M. Bhike, W. Tornow, Krishichayan, and A. P. Tonchev, Exploratory study of fission product yield determination from photofission of Pu 239 at 11 MeV with monoenergetic photons, Phys. Rev. C 95, 024608 (2017).
- [83] Krishichayan, S. W. Finch, C. R. Howell, A. P. Tonchev, and W. Tornow, Monoenergetic photon-induced fission cross-section ratio measurements for U 235, U 238, and Pu 239 from 9.0 to 17.0 MeV, Phys. Rev. C 98, 014608 (2018).
- [84] D. Habs and U. Köster, Production of medical radioisotopes with high specific activity in photonuclear reactions with γ -beams of high intensity and large brilliance, Appl. Phys. B **103**, 501 (2011).